8th International Conference on CFD in Oil & Gas, Metallurgical and Process Industries
SINTEF/NTNU, Trondheim Norway *CFD11-119*
21-23 June 2011

NUMERICAL SIMULATION OF LARGE BUBBLES IN CHANNELS USING A FRONT-TRACKING METHOD

Nicholas HOR[1,2]*, Jinsong HUA[1], Christopher J. LAWRENCE[1], Peter D.M. SPELT [2,3]

[1] Institute for Energy Technology, Process and Fluid flow Technology, PO Box 40, NO-2027 Kjeller, NORWAY

[2] Department of Chemical Engineering, Imperial College London, South Kensington Campus, London SW7 2AZ

[3]LMFA, CNRS, Ecully, France, and Department of Mechanical Engineering, Université de Lyon 1 (Claude Bernard), France

* E-mail: nick.hor@ife.no

ABSTRACT

Previous work on the motion of large bubbles in 2D channels in the creeping-flow limit is extended here to moderate Reynolds numbers ($10<Re<200$). Simulations are carried out to determine the effects of inertia, surface tension, viscosity and inclination angle on the terminal velocity in stagnant liquid, streamline patterns and bubble shape. Local wall shear stress and normal stress profiles are presented. Results are presented for a single large bubble (using a moving frame of reference) and a train of large bubbles (using a periodic cell). The method is validated against results from the literature.

Keywords: Multiphase flow, Taylor bubble, front-tracking method, wall shear stress, CFD.

NOMENCLATURE

Greek Symbols

κ Interface curvature, [1/m].
ρ Fluid density, [kg/m^3].
σ Surface tension coefficient, [N/m].
θ Inclination angle, [degree].
τ Time scale, [dimensionless].
μ Fluid viscosity, [kg/ms].

Latin Symbols

a Acceleration, [ms^{-2}].
Ar Archimedes number, [dimensionless].
Bo Bond number, [dimensionless].
D Characteristic length scale, [m].
d Bubble diameter, [m].
Fr Froude number, [dimensionless].
$\mathbf{g}$ Gravity, [m/s^2].
h Grid size, [m].
$\mathbf{n}$ Unit normal vector, [dimensionless].
p Pressure, [Pa].
Re Reynolds number, [dimensionless].
t Time, [s].
$\mathbf{u}$ Fluid velocity, [m/s].
$\mathbf{x}$ Position vector, [m].

Sub/superscripts

f A point on interface Γ.
l Liquid phase.
m Moving reference frame.
n Time step n.
p Point P.
σ Surface tension.
T Transpose operation.
$*$ Dimensionless number.
∞ Terminal.

INTRODUCTION

Slug flow is one of the most common flow patterns in oil/gas transport in pipelines. It is encountered when gas and liquid flow simultaneously in a pipe, over a certain range of flowrates. Slug flow is characterised by elongated bubbles which are separated by liquid slugs that contain dispersed small bubbles. Due to its complexity, it poses numerous challenges to experiments, numerical simulations and theoretical analysis. A simplified configuration of the fundamental interest of such flow is the case of an elongated bubble propagating in a channel in stagnant liquid.

The rise of a single bubble in stagnant or moving liquid in a vertical or an inclined pipe has been studied by researchers theoretically (Davies & Taylor 1950; Collins *et al*. 1978), experimentally (White & Beardmore 1962; Zukoski 1966; Maneri & Zuber 1974) and numerically (Miksis *et al*. 1981; Chen *et al*. 1999; DeBisschop *et al*., 2002). Early theoretical analyses were limited to vertical pipe flow with zero surface tension. The work of Cöuet & Strumolo (1987) provided a theoretical basis that both described the influence of surface tension and pipe inclination on the propagation velocity, but their work was limited to cases where the effect of viscosity in the liquid is negligible, i.e. $Re>200$ where the rise velocity of a large bubble is independent of Re (Zukoski 1966). The experimental results of White & Beardmore (1962) provided a comprehensive summary on the terminal velocity of a Taylor bubble

rising through stagnant liquid in a vertical tube. They identified the Bond number ($\rho_l g D^2/\sigma$), Froude number ($U_\infty/\sqrt{gD}$) and Morton number ($g\mu^4/\rho_l\sigma^3$) as useful dimensionless groups and concluded that viscous forces, interfacial effects and inertial effects are negligible if $\rho_l^2 g D^3/\mu^2 > 3\times10^5$, $Bo > 70$ and $Fr < 0.05$ respectively. Zukoski (1966) performed his experiments with bubbles of length at least 4 times the tube radius. He showed that the influence of surface tension was stronger than that of viscosity in the propagation speed of a long bubble. He also found that the bubble propagation velocity increased as the inclination was varied from horizontal to a critical angle of about 45° from the vertical where the velocity reached its maximum. The velocity then dropped as the angle was increased beyond the critical angle. The critical angle was not observed to be constant and was found to increase as *Bo* decreased. The effect of inclination angle on the rise velocity is complicated due to the changing shape of the bubble. The experimental results of Maneri & Zuber (1974) gave similar conclusions at high Reynolds numbers with different sets of parameters. Maneri & Zuber (1974) performed an investigation on two-dimensional bubbles and demonstrated that the motion of bubbles in inclined channels can be classified into three regimes. Furthermore, they showed that the wall effect decreases as the inclination is increased. Chen *et al*. (1999) considered a bubble rising in a closed vertical channel using a volume-of-fluid method which included surface tension forces. At low *Re* and *Bo*, they obtained bubbles with steady shape. However, the bubbles formed an upside-down U shape and then broke apart at higher values of either or both non-dimensional numbers. DeBisshop *et al*. (2002) performed a two-dimensional study using a boundary integral method for bubbles rising in Stokes flow. They observed that increasing *Bo* increased the deformation, and hence the terminal velocity of the bubble. They also reported that there was a critical Bond number beyond which no steady bubbles were found.

In this paper we study the dynamics of bubbles rising in vertical and inclined channels, in an air-water system beyond the Stokes flow regime. A front tracking method is used for this purpose (Hua *et al*. 2008). Simulations were performed using a range of *Bo* (5<*Bo*<50), *Re* (10<*Re*<200) and channel inclination of 0° to 90°. In this range of parameters, surface tension, viscous and inertial effects are all important to the bubble dynamics. This study is mainly focused on examining the effect of the above parameters on the terminal velocity, steady state shape, wall shear stress and normal stress of a bubble.

MODEL DESCRIPTION

The schematic of a large bubble rising in an inclined channel is shown in Fig. 1. The large bubble is initially ellipsoidal and is at rest. The void fraction in the regions of gas and liquid are set to be 1 and 0 respectively. Fig. 1 shows the Cartesian coordinate system (*x*,*y*) with the *y* axis normal to the channel walls and *x* axis parallel to them. The channel is inclined at an angle θ from the horizontal axis.

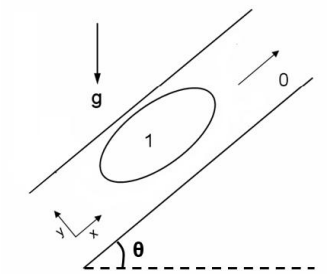

Figure 1: Schematic of bubble rising in an inclined channel

Front tracking method

Governing equations

The slug flow system is represented herein as an isothermal, two-fluid system with two incompressible and immiscible Newtonian fluids. A single set of governing equations is used for the entire computational domain, where different phases are treated as one single fluid with varying physical properties across the interface (Brackbill *et al*. 1992; Tryggvason *et al*. 2001). Under the concept of the "one-fluid" approach, the governing equations for gas-liquid two-phase flows can be derived. The mass balance for the whole flow domain is

$$\nabla\cdot\mathbf{u} = 0, \tag{1}$$

and the momentum balance is

$$\begin{aligned}&\frac{\partial(\rho\mathbf{u})}{\partial t} + \nabla\cdot\rho\mathbf{u}\mathbf{u} = -\nabla p + \nabla\cdot\left[\mu(\nabla\mathbf{u}+\nabla^T\mathbf{u})\right]\\ &+\int_\Gamma \sigma_f\kappa_f\mathbf{n}_f\delta(\mathbf{x}-\mathbf{x}_f)ds + (\rho-\rho_l)\mathbf{g}\end{aligned} \tag{2}$$

Interfacial terms involve the two-dimensional δ-function $\delta(\mathrm{x}) = \delta(x)\delta(y)$ at the interface between the two phases. Fluid properties such as density and viscosity in each phase are constant but are discontinuous across the interface. Equation (2) can be non-dimensionalised by introducing dimensionless characteristic variables shown below:

$$\mathbf{x}^* = \mathbf{x}/D,\ \mathbf{u}^* = \mathbf{u}/\sqrt{gD},\ \tau^* = t\sqrt{g/D},\ \rho^* = \rho/\rho_l,$$
$$p^* = p/\rho_l gD,\ \mu^* = \mu/\mu_l,\ \kappa^* = D\kappa,\ \mathrm{g}^* = \mathrm{g}/g$$

where $g = \|\mathbf{g}\|$. Substituting the above variables, equation (2) becomes:

$$\begin{aligned}&\frac{\partial(\rho\mathbf{u})}{\partial t} + \nabla\cdot\rho\mathbf{u}\mathbf{u} = -\nabla p + \frac{1}{Ar}\nabla\cdot\left[\mu(\nabla\mathbf{u}+\nabla^T\mathbf{u})\right]\\ &+\frac{1}{Bo}\int_\Gamma \kappa_f\mathbf{n}_f\delta(\mathbf{x}-\mathbf{x}_f)ds + (\rho-1)\mathbf{g}\end{aligned} \tag{3}$$

Here, the * decoration has been removed for convenience. The dimensionless Archimedes (*Ar*) and Bond number (*Bo*) are defined as $Ar = \rho_l g^{0.5} D^{1.5}/\mu_l$ and $Bo = \rho_l g D^2/\sigma$ respectively. The Archimedes number is expressed as a ratio of buoyancy to viscous forces to characterize the rise of a bubble in liquid due to buoyancy. The Bond number is a measure of the importance of surface tension compared to the gravity acting on the rising bubble. In order to facilitate a comparison with other work, we note that further

dimensionless groups commonly used are the bubble Reynolds number $\mathrm{Re}=\rho_l D U_\infty/\mu_l$ and the Froude number, $Fr=U_\infty/\sqrt{gD}$. These are related through *Re=Ar·Fr*.

Discontinuities across the interface

Since each fluid is assumed incompressible, it is reasonable to assume that the fluid properties are constant in each phase and as a result the properties are physically discontinuous across the interface between the two immiscible fluids. This sudden jump of fluid properties at grid points in the vicinity of the interface has traditionally caused numerical diffusion and instability in numerical methods. The front tracking method uses a fixed background mesh to solve the governing equation and a separate mesh to track the position of the interface explicitly as well as the discontinuities across the front (Tryggvason *et al*. 2001). Unverdi & Tryggvason (1992) suggested that the difficulties caused by the discontinuities can be overcome by introducing an artificial finite thickness of the order of the mesh size instead of zero thickness for the interface. The thickness is kept constant during the computation. The discontinuities across the front are distributed from the front mesh to the background mesh so that continuous distributions of the fluid properties can be reconstructed on the fixed background grid. Consequently, the fluid properties change smoothly and continuously across the interface. The front tracking method therefore does not exhibit numerical diffusion across the interface. In order to achieve this, the δ-function, which represents the discontinuities of fluid properties across the interface, is approximated by a continuous distribution function $D(\mathbf{x})$. It describes the fraction of interfacial quantities such as density difference, viscosity difference between the two phases and the surface tension, being distributed to nearby grid points across the artificial thickness of the interface. In this work the Peskin distribution function is adopted (Peskin 1977):

$$D(\mathbf{x}-\mathbf{x}_f)=\begin{cases}(4h)^{-2}\prod_{i=1}^{2}\left(1+\cos\left(\frac{\pi}{2h}|\mathbf{x}-\mathbf{x}_f|\right)\right) & \text{if } |\mathbf{x}-\mathbf{x}_f|<2h\\ 0, & \text{otherwise}\end{cases} \quad (4)$$

Using the same distribution function, the singular source term due to surface tension on the interface is distributed to the background grid in accordance with the geometry of the interface. The governing equations are then solved on the fixed background grid using a preferred numerical approach. Further details of the methodology for the redistribution of fluid properties across the interface were discussed in Hua *et al*. (2008) and Tryggvason *et al*. (2001).

Tracking the moving interface

Adaptive front markers are used to represent the interface between the two fluid phases. The velocity $\mathrm{u}_f(\mathrm{x}_f,t)$ of the moving front markers is then obtained by interpolating from the flow field on the fixed background grid. The front marker points are advected in a Lagrangian manner from position $\mathbf{x}_f^n$ at the *n*th time step to a position $\mathbf{x}_f^{n+1}$ at the *(n+1)*th time step.

$$\mathrm{u}_f(\mathrm{x}_f,t)=\sum_{\mathrm{x}}\mathrm{u}(\mathrm{x},t)D(\mathrm{x}-\mathrm{x}_f) \quad (5)$$

$$\mathrm{x}_f^{n+1}=\mathrm{x}_f^n+\mathrm{u}_f^n\Delta t \quad (6)$$

The mesh quality may deteriorate as the front marker points are advected. Therefore, the front mesh size is checked and mesh adaptation is performed at every time step. In addition, a CFL check was performed throughout the whole computational time for all simulations to ensure the stability of the calculations.

Flow solver

The projection-correction and SIMPLE methods are the two most common numerical methods for a "one-fluid" formation. The explicit projection-correction has been conventionally employed with front tracking methods. However, Bunner & Tryggvason (2002) reported that results generated by this explicit method have been limited to flows with low to intermediate Reynolds numbers and small density ratios. Hua & Lou (2007) implemented a modified version of the semi-implicit SIMPLE method for axisymmetric multiphase flow and their results showed that this approach can robustly solve the Navier-Stokes equation with large density ratios up to 1000 and large viscosity ratios up to 500. The system for which the simulations were reported in the paper was an air-water system, and so the SIMPLE algorithm is an obvious choice.

Moving reference frame

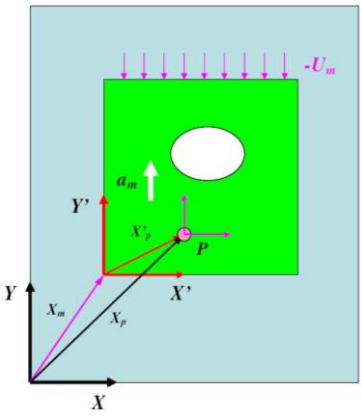

Figure 2: Schematic of moving reference frame (Hua *et al*. 2008)

In order to study the long-term behaviour of the flow and evolution of the moving interface between the fluids without having a large computational domain, a moving frame of reference (MRF) is used in our simulations. The idea is to move the reference frame together with the large bubble so that the bubble is (almost) stationary with respect to time in the solution domain. The size of the computational domain may then be chosen regardless of the computational time and the computational cost can be greatly reduced. A MRF is shown in Fig. 2. The frame *XY* is stationary and the frame *X'Y'* is moving. The positions of the point P in *XY* and *X'Y'* are denoted by $\mathbf{x}_p$ and $\mathbf{x}_p'$ respectively. The position of the MRF is denoted by $\mathbf{x}_m$.

The velocity of point P is $\mathbf{u}(\mathbf{x},t)$ and $\mathbf{u}'(\mathbf{x}_p',t)$ in the frames *XY* and *X'Y'* respectively. The velocity of the moving frame is denoted by $\mathbf{u}_m(t)$. The following equations can then be obtained.

$$\mathbf{x}_p = \mathbf{x}_m + \mathbf{x}_p' \tag{7}$$

$$\mathbf{u}(\mathbf{x},t) = \mathbf{u}_m(t) + \mathbf{u}'(\mathbf{x}_p',t) \tag{8}$$

Allowing for translational, but not rotational, movement of the reference frame, the governing equation is modified for the moving reference frame:

$$\frac{\partial(\rho\mathbf{u}')}{\partial t} + \nabla'\cdot\rho\mathbf{u}'\mathbf{u}' + \rho\frac{d\mathbf{u}_m}{dt} = -\nabla' p + \frac{1}{Ar}\nabla'\cdot\left[\mu(\nabla'\mathbf{u}' + \nabla'^{T}\mathbf{u}')\right] + \frac{1}{Bo}\int_\Gamma \kappa_f \mathbf{n}_f \delta(\mathbf{x}' - \mathbf{x}_f')ds + (\rho-1)\mathbf{g} \tag{9}$$

$$\nabla'\cdot\mathbf{u}' = 0 \tag{10}$$

As the MRF is generally accelerating with the moving front, the governing equation is no longer solved in an inertial frame and therefore the momentum balance has to be modified to take the acceleration of the moving frame into account. Furthermore, according to equation (8), the velocity condition on the boundary $\mathbf{x}_B'$ must be modified as follows:

$$\mathbf{u}'(\mathbf{x}_B',t) = \mathbf{u}(\mathbf{x}_B,t) - \mathbf{u}_m(t) \tag{11}$$

The additional term $d\mathbf{u}_m/dt$ on the left hand side of equation (9) denotes the acceleration $\mathbf{a}_m$ of the moving frame of reference. The value of $\mathbf{a}_m$ should be chosen so that the acceleration of the moving frame equals the acceleration of the bubble (Rusche 2002; Hua *et al.* 2008).

NUMERICAL METHOD

In the present simulations, the length of the computational domain is at least three times larger than the channel width. Pressure inlet and outlet boundary conditions are employed at the boundary of the computational domain. The pressure p and normal pressure gradient $\partial p/\partial n$ are set to be zero at the inlet and outlet respectively. The horizontal velocity component at the inlet has a zero normal gradient $\partial u/\partial n = 0$ and the vertical component is set to be zero. At the outlet, the horizontal velocity is set to zero when the liquid is stagnant. As an alternative to these boundary conditions, a periodic boundary condition (PBC) is also used to represent a train of bubbles, i.e., to 'recycle' the flow that exits from one side of the computational domain back to the other side. To achieve this, velocities at the last two grid lines at the outlet are set to be equal to those of the first two grid lines at the inlet. The purpose of PBC must not be confused with that of MRF. While the MRF allows a short computation domain to be implemented when the physical domain is long, the PBC represents a series of large bubbles hence capturing the physics of slug flow more realistically. When the PBC is used, the pressure gradient over the computational domain is set to a selected value so that the liquid moves forward. The chosen pressure gradient is large enough for the elongated bubble to move in the horizontal channel but small enough not to break the interface and jeopardize the stability of the simulation.

To solve the Navier-Stokes equations, a fixed, regular staggered grid is employed and the momentum equations are discretized using a finite volume method. After the front has been advected explicitly for a time step, the fluid properties and the surface tension force are updated. The coupled flow velocity and pressure are then updated by solving the momentum and continuity equations using the SIMPLE algorithm (Patankar 1980). To advance the solution from one time step to the next, the velocity of the front marker points $\mathbf{u}_f^n$, is evaluated through interpolation of the fluid velocity field $\mathbf{u}^n$ using equation (5). With the known interface velocity $\mathbf{u}_f^n$, the front is advected to its new position $\mathbf{x}_f^{n+1}$ using equation (6). At the new interface positions, the redistribution of the interfacial properties is performed with the Peskin distribution function from equation (4). Subsequently, the fluid property distributions for the next time step are updated on the grid points. With appropriate boundary conditions, the new velocity field $\mathbf{u}^{n+1}$ and the pressure p^{n+1} can be obtained by solving the continuity and momentum equations using the SIMPLE algorithm.

RESULTS

In this section, we validate the code and examine the effect of the angle of inclination, Bond number, Reynolds number and bubble size on the terminal velocity, bubble shape, and the distributions of wall shear stress and normal stress. The effect of the applied pressure gradient for simulations with periodic boundary condition is also investigated. Unless specified otherwise, all the simulations were carried out for an air-water system with $\mu/\mu_l = 0.01$ and $\rho/\rho_l = 0.001$.

Table 1: Simulation matrix.

Dp	Re	Bo	Angle							
Stagnant liquid										
-	10	10	0	-	-	-	-	-	-	-
-	20	5	0	10	30	50	60	70	85	-
-		10	0	10	30	50	60	70	85	-
-		20	0	10	30	50	60	70	85	-
-		30	0	10	30	50	60	70	85	-
-		50	0	10	30	50	60	70	85	-
-	50	10	0	-	-	-	-	-	-	-
-	100	10	0	-	-	-	-	-	-	-
-	200	5	-	10	30	50	60	70	85	-
-		10	0	10	30	50	60	70	85	-
-		20	0	10	30	50	60	70	85	-
-		30	0	10	30	50	60	70	85	-
-		50	0	10	30	50	60	70	85	-
Liquid flow with PBC										
0.0	20	5	0	-	-	50	-	-	85	-
		10	0	-	30	50	60	-	85	-
		20	0	-	-	50	-	-	85	-
		30	0	-	-	50	-	-	85	-
1.0	20	5	0	-	30	50	60	-	-	90
		10	0	-	30	50	60	-	-	90
		15	0	-	30	50	60	-	-	90
		20	0	-	30	50	60	-	-	90

The domain length is 3, 6 or 12 times the width of the channel. The initial shape of the bubble is an ellipse of aspect ratio 2.5 or 7.5 and area 0.4π or 1.2π. The bubble

is initially centred in the middle of the channel. In this paper, bubbles with higher aspect ratio are regarded as long bubbles and those with lower aspect ratio are said to be large bubbles. We validate our code by comparing our results with DeBisschop *et al*. (2002) for small Reynolds number. Then, we begin our investigation by performing a parametric study of the aforementioned parameters for a large bubble in stagnant liquid, followed by a similar study for a large bubble propagating under periodic boundary condition. Table 1 indicates the number of simulations that have been performed for large bubble. Some of the simulations in Table 1 were repeated for long bubbles. Due to the overwhelming amount of data, only key results are presented in this paper.

Validation

The validation cases were carried out using the parameters in the work of DeBisschop *et al*. 2002. They investigated the dynamics of a gas bubble rising through an inclined channel in two dimensions in the Stokes flow limit using a boundary integral method with PBC. The periodicity was equal to three and the initial bubble shape was a circle with diameter of 0.9. The following parameters are used: $\mu/\mu_l = 1.0$, $\rho/\rho_l = 0.001$, *Bo*=10 and *Re*=1.0. Fig. 3 and 4 shows the result of the validation study for the bubble shape and terminal velocity at different angle of inclination θ. As can be seen from the figures, although DeBisschop *et al.* (2002) performed their simulations in the Stokes flow limit where the Reynolds number is vanishingly small, the steady state bubble shape and the terminal velocity predicted from our simulation with *Re*=1.0 under the same *Bo*, viscosity and density ratios are in good agreement with those of DeBisschop *et al*. (2002). The small discrepancy in the bubble shape is due to the fact that a coarse grid of 60x20 and a different *Re* was used here.

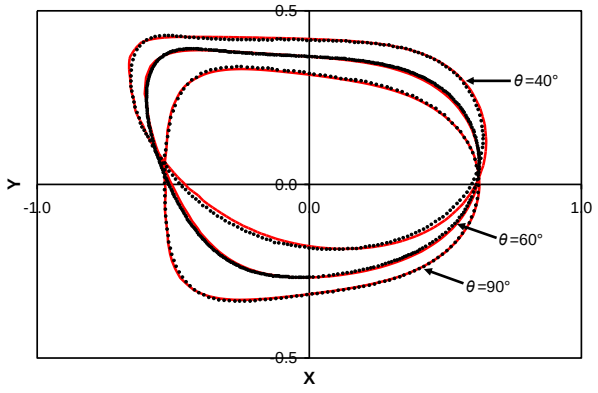

Figure 3: Comparison of steady state bubble shape with DeBisschop *et al*. (2002) (represented by dots). *Re*=1.0, viscosity ratio equals 1.0 at different channel inclination. The red line represents the bubble shape of our model.

To test the effect of *Re* on bubble shape and velocity, simulations at *Re*=1.0 and 2.0 were performed with a different grid size. As can be seen from Fig. 5(a), the shape of the bubbles from our model is almost identical even though the terminal velocity at *Re*=2.0 is approximately double of that at *Re*=1.0. This shows that the bubble shape is relatively insensitive to the changes in *Re* compared to the terminal velocity. On the other hand, the grid refinement only exhibits a tiny effect on the bubble shape as can been from Fig. 5(b). The terminal velocity for the simulation with a coarser grid is approximately 5% less than that with a finer grid. This suggests that grid refinement can improve the accuracy of the prediction of the terminal velocity but may not necessarily have a significant effect on the bubble shape.

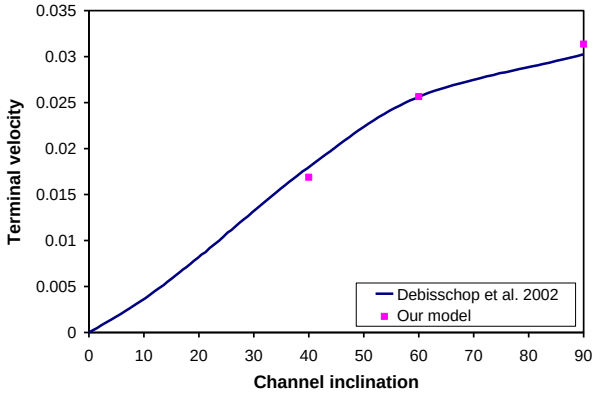

Figure 4: Comparison of terminal velocity with DeBisschop *et al*. (2002). *Re*=1.0, viscosity ratio equals 1.0 at different channel inclination.

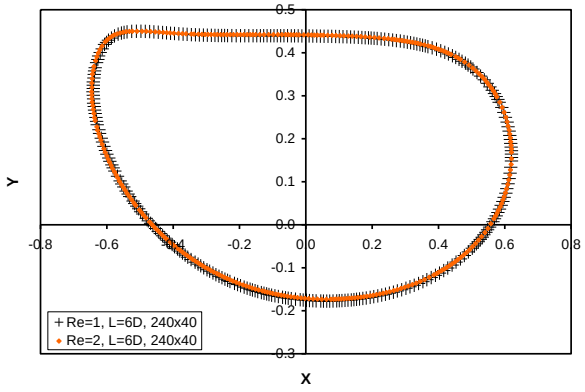

(a)

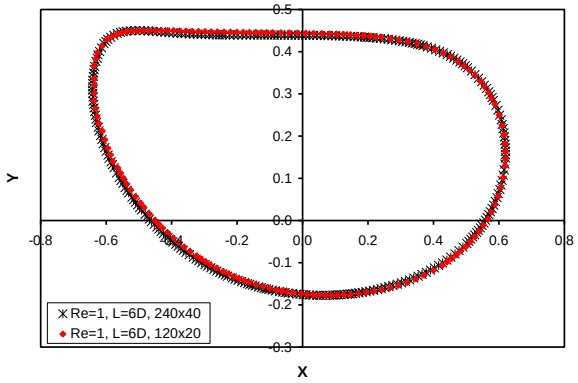

(b)

Figure 5: Comparison of steady state bubble shape between (a) our simulation of *Re*=1.0 and *Re*=2.0 at θ=40° from the horizontal axis and (b) our simulation with different grid size at θ=40° from the horizontal axis. *Re*=1.0.

Fig. 6 shows the effect of domain size on the bubble shape. The bubble is closer to the top wall for L=6D than that for L=3D and is slightly shorter. The bubble shape for L=3D is very close to DeBisschop *et al*. (2002) even though the grid is coarse. The terminal velocity for the case of L=6D is approximately 40%

lower than that for the case of L=3D. Our simulations for other channel inclinations show that the difference of terminal velocity increases significantly with increasing θ.

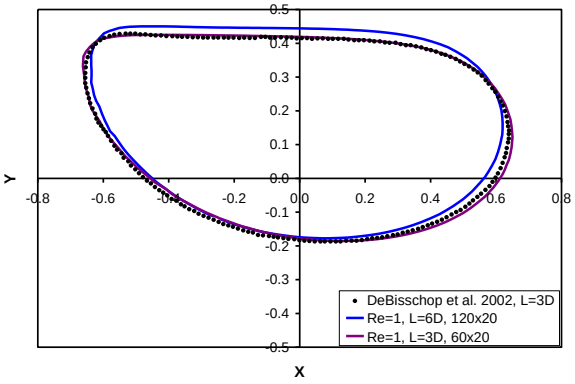

Figure 6: Comparison of steady state bubble shape between DeBisschop *et al*. (2002) and our model with different domain size at θ=40° from the horizontal axis.

Sensitivity analysis for a single bubble rising in stagnant liquid (without PBC) showed that the simulation results can be safely determined to be independent of the domain size, magnitude of each time step and the initial bubble shape since the terminal velocity from these runs were within 1% of the value of the reference case. Confidence of grid independence is gained from selected runs that were completed with 360x60, 480x80 instead of the usual grid of 240x40. The results are very similar. In addition, the terminal velocity for the runs changed by less than 1% upon grid refinement.

Streamlines and bubble shape

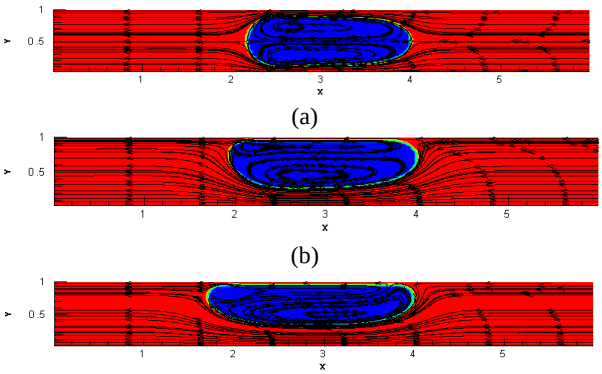

Figure 7: Streamlines for bubbles of area 0.4π at (a) θ=90°, (b) θ=40°and (c) θ=5° at *Re*=20 and *Bo*=10.

Fig. 7 shows streamlines for θ=90°, θ=40°and θ=5° at *Re*=20 and *Bo*=10 with no PBC. It can be seen from the plot that the symmetry of the streamlines is lost in the case of θ=5° and θ=40°. The liquid tends to go along the lower wall and recirculate back to the centreline of the bubble. The two eddies inside the bubble at θ=90° are of the same size. The bullet-shaped bubble occupies most of the channel and has a rounded bottom rather than a flat one. This indicates that the surface tension is holding the bubble in shape. At θ=5°, the eddy at the bottom right side of the bubble is larger than that for θ=90° and the eddy at the top of the bubble is reduced. The bubble becomes asymmetrical due to elongation of the bubble tail and it is closer to the top wall when compared to the bubble rising at θ=90°. There is a larger gap between it and the lower wall hence it blocks less of the channel. The side next to the top wall is also noticeably much flatter. The observations support the explanation for the trend of the effect of channel inclination on the bubble terminal velocity in Fig. 8 below.

Effect of Bond number

Stagnant liquid

Simulations were carried out according to Table 1 to facilitate the study of the effect of *Bo* and channel inclination on the bubble velocity at steady state. It was noticed that the time for the bubble to reach steady states decreases as the angle increases. It can be seen from Fig. 8 that *Fr* increases with *Bo* at a fixed *Re* regardless of the channel inclination. This suggests that as the surface tension decreases, the terminal velocity of the bubble increases and this is consistent with previous experimental work (Zukoski, 1966). Zukoski (1966) showed that the influence of surface tension was stronger than that of viscosity in the determination of the velocity for a long bubble. Comparing the case of *Re*=20, *Bo*=20 (red line) and *Re*=200, *Bo*=5 (blue dotted line) with the case *Re*=20, *Bo*=5 (blue line) as a reference, it can be noticed that by increasing *Bo* four times, the propagation rate is higher than increasing *Re* by ten times, regardless of channel inclination. This observation is in agreement with Zukoski (1966).

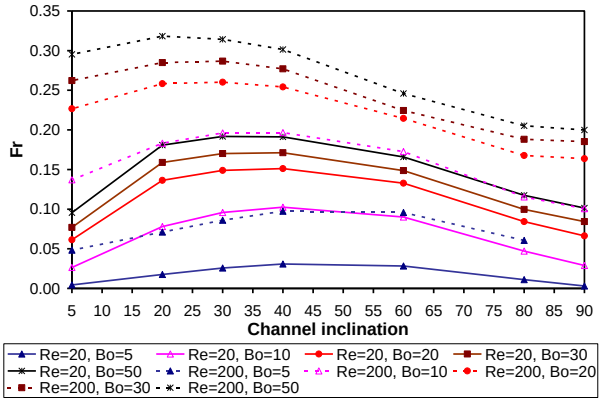

Figure 8: Plot of *Fr* vs. channel inclination for 5<*Bo*<50.

It can also be observed that the terminal velocity of a bubble increases as the channel inclination increases from horizontal to a critical angle where the velocity reaches a maximum and then drops as the inclination angle is increased beyond the critical angle. It is interesting to see that the critical inclination angle at which the maximum propagation rate occurs decreases with *Bo*. This observation is also consistent with Zukoski (1966) and Shosho & Ryan (2001). At *Re*=20 and *Re*=200, the respective critical channel inclination decreases from 40° to 30° and 40° to 20° for an increase of *Bo* from 5 to 50. At a given *Re*, the gap between the lines is diminishing and this suggests that the influence of surface tension on the propagation velocity reduces as *Bo* increases. It is possible that eventually the surface tension has no further effect on the bubble velocity when *Bo* is sufficiently large. This prediction was proven theoretically by Couët & Strumolo (1987) (see their Fig.

7). In fact, in the case of *Re*=200, *Bo*=50 and θ=90° of our model, the terminal velocity is less than 10% smaller than the limiting velocity for a vertical pipe with large *Bo* in the work of Couët & Strumolo (1987).

Fig. 7(a), (b) and (c) can be used to identify possible explanations for the trends in Fig. 8. When the elongated bubble propagates along a channel in stagnant liquid, the liquid in front of the bubble is transported to the back of the bubble. The buoyancy force gives the bubble forward motion and it experiences the effect of drag which acts against the direction of motion. At steady state the buoyancy and the drag must balance. In a vertical channel, the bubble occupies most of the channel, leaving only two narrow liquid layers for liquid to move from the bubble nose to bubble tail region. The liquid transport is so inefficient that even though the buoyancy of the bubble is the strongest in a vertical channel, the terminal velocity is smaller than that for a bubble rising in an inclined channel. In an inclined channel, the bubble occupies less cross-sectional area than in a vertical channel. It rises towards the upper wall and it leaves a much wider gap for liquid transport. The efficiency of liquid transport improves significantly, so that even though the buoyancy on a bubble decreases in an inclined channel, the bubble rises faster than in a vertical channel. This explains the peaks in Fig. 8. Further decrease of channel inclination results a reduction of velocity when the inclination angle is smaller than the critical angle. In the case of θ=5° for instance, the thickness of the liquid layer is the largest among all inclinations examined in this work. Although the liquid transport is the most efficient in this case, the buoyancy is so weak that the bubble rises more slowly along the channel. While the buoyancy in the x-direction depends on a sine function and it drops significantly at small angles, the change of the narrowest width of the liquid layer drops from 60% to 22% as θ decreases from 90° to 40° and from 40° to 5° respectively.

Moving liquid with periodic boundary condition

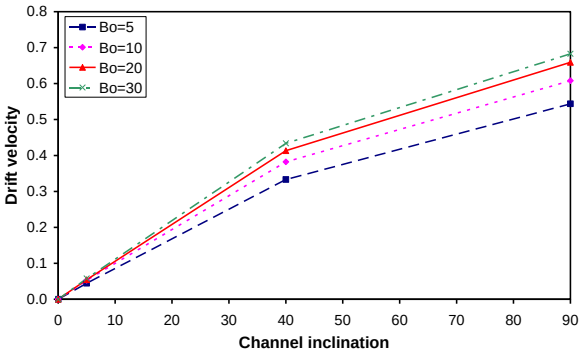

Figure 9: Plot of drift velocity vs. channel inclination for 5<*Bo*<30 with pressure drop equal 0.0.

In order to model a train of bubbles PBC were imposed. In this case, the appropriate boundary condition is the pressure drop over the computational domain. Fig. 9 shows the effect of *Bo* and channel inclination on the drift velocity of the bubble when the pressure gradient equals zero and *Re*=20. The drift velocity is the steady state velocity of a bubble minus the average of the horizontal component of liquid velocity over the whole domain. This is to take away the significant contribution of liquid velocity on the bubble velocity. As can be seen from Fig. 9 the drift velocity increases with *Bo*. This result is consistent with that for a single bubble rising in stagnant liquid without PBC. The drift velocity of a bubble is zero when the channel is horizontal. The drift velocity increases with the channel inclination and reaches a maximum at θ=90°. The same observation was reported both numerically (DeBisschop *et al*. 2002) and experimentally (Masliyah *et al*. 1994) for low *Re*.

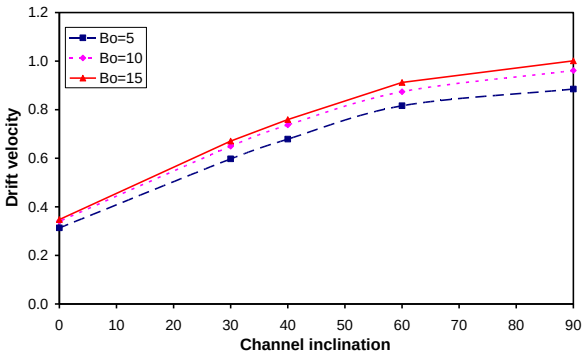

Figure 10: Plot of drift velocity vs. channel inclination for 5<*Bo*<15 with pressure drop equal 1.0.

Fig. 10 shows the effect of channel inclination and *Bo* on the drift velocity when the pressure drop is set to 1.0. In general, the trend is similar to Fig. 9 but drift velocities increase due to the pressure drop. The effect of the pressure drop can be observed when the channel is horizontal (θ=0°) since the buoyancy force is not a driving force for the bubble propagation in this case. The pressure drop increases the drift velocity by about 0.3-0.35 across the range of Bond numbers and channel inclinations.

Effect of Reynolds number

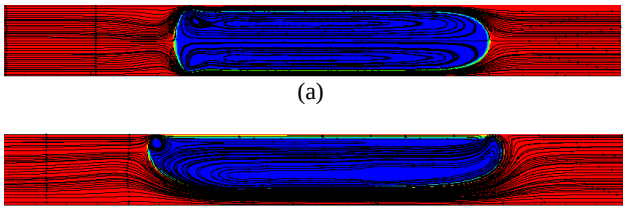

(a)

(b)

Figure 11: Streamlines for bubble of area 1.2π at (a) θ=90° and (b) θ=5° at *Re*=200 and *Bo*=10.

The investigation of the effect of *Re* on *Fr* was carried out by running simulations for single long bubbles rising in a vertical channel at a fixed *Bo*. Fig. 11 shows a long bubble in a vertical and an inclined channel. The plot of *Fr* as a function of *Re* for 10<*Re*<200 and *Bo*=10 when the bubble is at steady state is shown in Fig. 12. The bubble is determined to be at steady state if the velocity changes less than 1% within 3000 time steps. No steady state bubble shape and velocity were observed for *Re*>200. In some cases where *Re*>200, the bubbles formed an upside-down U shape and eventually broke apart. The same type of bubble shape was also observed by Chen *et al*. (1999).

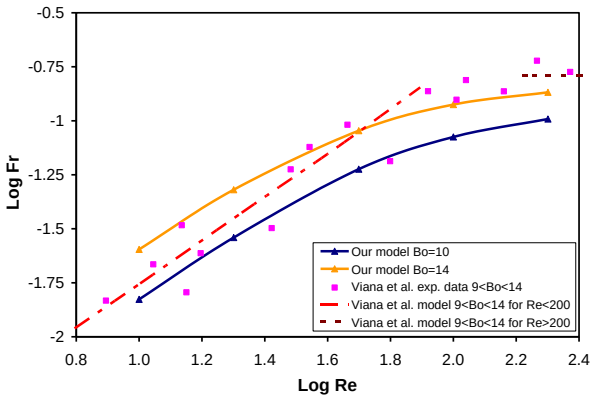

Figure 12: Plot of log *Fr* vs. log *Re* for *Bo*=10 and *Bo*=14 in vertical channel.

Our model shows (see Fig. 12) that the steady state velocity of a bubble increases non-linearly with *Re*. The slope of the graph decreases when *Re* increases and is expected to flatten out when *Re*>200. The terminal velocity seems to converge to an asymptotic value when *Re* is large. Viana *et al*., (2003) stated that the bubble velocity is linearly proportional to *Re* when *Re*<10 and independent of *Re* when *Re*>200 and in between is the transition region. The data of Viana *et al*., (2003) for 9<*Bo*<14 in the transition region are plotted in Fig. 12 for comparison. The red dashed line and the brown dotted line are the best-fits of their experimental data for *Re*<100 and *Re*>200 respectively. As can be seen from the figure the data are quite scattered and our model with *Bo*=10 slightly underpredicts the steady state velocity for 9<*Bo*<14. Although a two-dimensional model can give reasonable predictions of the bubble motion in vertical tubes due to the symmetry, we should not expect precise quantitative agreement. This will be assessed in our future work on three-dimensional simulations. On the other hand, the experimental data cover a range of *Bo* and it is possible that most of the data refer to the upper limit of the range. However, our model has a fixed *Bo* and this could be a reason for the underprediction. In order to examine this argument, a series of simulations were run for 10<*Re*<200 and *Bo*=14 and the result is represented by the orange solid line in Fig. 12. A majority of the experimental data for 9<*Bo*<14 and log *Re*<1.9 are inside the area between the two solid lines. For log *Re*>1.9, the underprediction must be attributed to the fact that these simulations are for 2D systems. In general, it can be seen that our model, though it is a two-dimensional model, is able to give reasonable qualitative predictions for a bubble rising in a pipe for log *Re*<1.9 and 10<*Bo*<14.

Wall shear stress and normal stress

Fig. 13 shows the local wall shear stress as a function of *x* for the case shown in Fig. 11(a). The position *x* is normalised by the diameter of the channel. The wall shear stress is defined as $\mu_l \, du/dy$(made dimensionless here with $\mu_l \sqrt{g/D}$). Due to the symmetry of the vertical case, only the wall shear stress profile of the top wall of the computational domain is shown. The dotted pink line shows the *y*-averaged void fraction along the *x*-axis. From Fig. 13, it can be seen that at *x/D*=5.25 and 10.0, there are smooth transitions of the wall shear stress at the back and front of the bubble. It is also noted that the higher the void fraction, the thinner the film thickness. There is a region where the local wall shear stress is almost independent of *x/D*. This reflects a fully developed condition in the liquid layer. The local wall shear stress reaches a maximum at the bubble tail where the void fraction is the highest. The liquid velocity exhibits a rapid change at the bubble tail when the liquid jet penetrates to the bubble wake. This gives a higher velocity gradient than that in the bubble body and hence higher local wall shear stress.

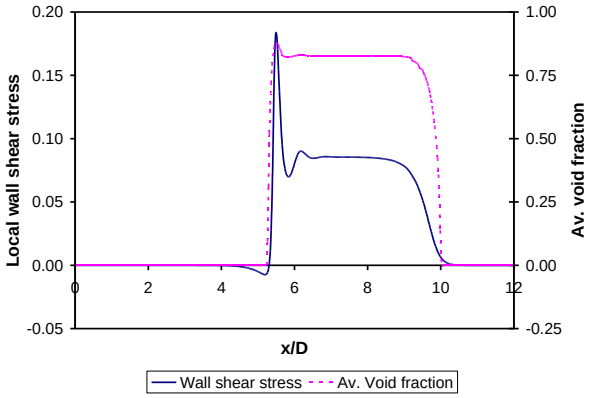

Figure 13: Local wall shear stress and void fraction profiles for a bubble of area 1.2π with *Re*=200, *Bo*=10 and θ=90°. See Fig. 11(a).

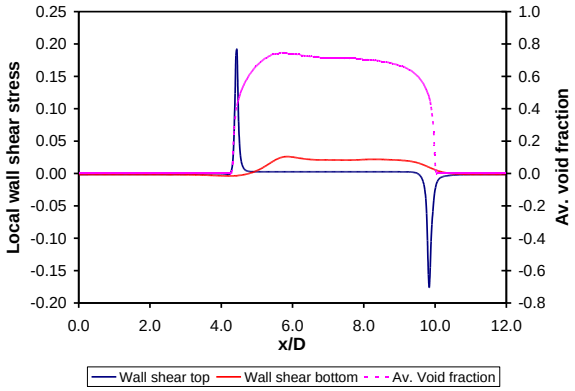

Figure 14: Local wall shear stress and void fraction profiles for a bubble of area 1.2π with *Re*=200, *Bo*=10 and θ=5°. See Fig. 11(b).

Fig. 14 shows the local wall shear stress as a function of *x* for the case shown in Fig. 11(b). The black and the red line correspond to the local wall shear stress at the top and bottom of the channel respectively. Fig. 14 shows that the local wall shear stress at the bottom of the channel is in general higher than that of the top of the channel. However, the maximum wall shear stress at the bottom of the channel is significantly lower than that of the top of the channel. There is a sharp peak at the bubble tail which is consistent with Fig. 13. Interestingly, the peaks in shear stress can possibly have an effect on the corrosion rate, helping to ripped off corrosion films and expose fresh metal (Langsholt *et al*. 2002).

Fig. 15 shows the profiles of normal stress and pressure at the wall for the case shown in Fig. 11(a). The normal stress in this figure corresponds to the normal

stress at the top of the channel. The normal stress consists of two components, pressure and normal viscous stress: $-(p-p_{ref})+\mu_l\, dv/dy$. The magnitude of the normal viscous stress is O(10^{-2}) whilst the pressure is O(1) therefore the contribution of normal viscous stress to the normal stress is small. Comparing with the wall shear stress, the normal viscous stress is noticeably smaller. Notice that there is a spike at the bubble tail but not at the bubble nose. The spike is associated with the increase of the velocity in the *y*-direction when the liquid jet penetrates to the bubble wake. A spike was also observed in the experiments by Langsholt *et al.* (2003). They reported two peaks in *dp/dx* within the slug body, one larger peak at the bubble tail and one smaller peak near the bubble nose.

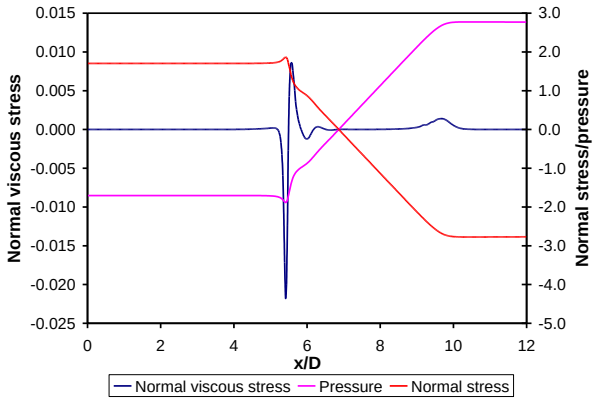

Figure 15: Normal stress and pressure profiles for a bubble of area 1.2π with *Re*=200, *Bo*=10 and θ=90°. See Fig. 11(a).

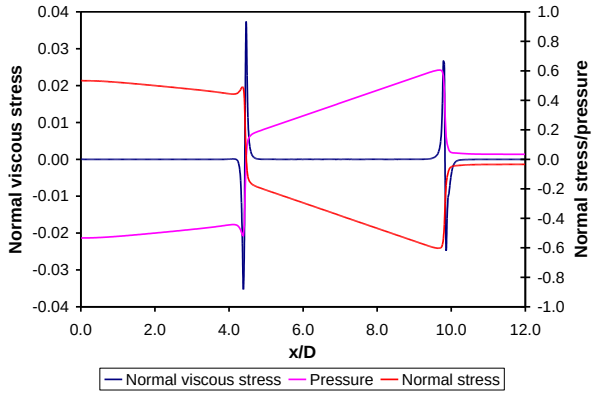

Figure 16: Normal stress and pressure profiles for a bubble of area 1.2π with *Re*=200, *Bo*=10 and θ=5°. See Fig. 11(b).

Fig. 16 shows the profiles of normal stress and pressure at the wall for the case shown in Fig. 11(b). The normal stress in this figure corresponds to the normal stress at the top of the channel. It is expected that the normal stress in this case is significantly lower than that for a bubble rising in a vertical channel because the hydrostatic pressure experienced by the bubble rising in vertical channel is higher than the bubble rising in an inclined channel. Comparing Fig. 15 and 16, the normal viscous stress for the case of θ=5° is higher than that for θ=90° at both the bubble nose and tail. Furthermore, the normal viscous stress for the case of θ=5° has a larger contribution to the normal stress compared to the case of θ=90°. However, the normal viscous stress is still O(10) smaller than the pressure and the normal stress is still dominated by the pressure.

CONCLUSIONS

A front tracking method has been implemented to study the effect of *Re*, *Bo* and channel inclination on the shape and terminal velocity of a large bubble. The terminal velocity of a single bubble increases with *Bo* regardless of channel inclination and *Re*. It also increases with channel inclination until a critical inclination is reached. Beyond the critical angle, the terminal velocity drops as the inclination angle increases further. The critical inclination is not constant and it depends on the value of *Bo*.

Trains of bubbles are simulated using periodic boundary condition. The effect of channel inclination on the steady state drift velocity is different from that for a bubble rising in stagnant liquid. A critical inclination does not exist in this case. However, the effect of *Bo* on the drift velocity is consistent with simulations for single bubbles.

The effect of channel inclination on the terminal velocity is complex due to the change of bubble geometry. The balance of the driving force (buoyancy) and retarding force (drag) changes with the bubble shape. The local wall shear stress reaches its maximum value at the bubble tail regardless of channel inclination. The normal viscous stress remains small compared to the shear stress and the pressure.

REFERENCES

BRACKBILL, J.U., KOTHE, D.B., ZEMACH, C., (1992). "A continuum method for modeling surface-tension", *Journal of Computational Physics* **100**, 335-354.

BUNNER, B. and TRYGGVASON, G., (2002). "Dynamics of homogeneous bubbly flows Part 1. Rise velocity and microstructure of the bubbles", *Journal of Fluid Mechanics*, **466**, 17-52.

CHEN, L., GARIMENLLA, S., REIZES, J., LEONARDI, E., (1999). "The development of a bubble rising in a viscous liquid", *Journal of Fluid Mechanics*, **387**, 61-96.

COLLINS, R., DEMORAES, F.F., DAVIDSON, J.F., HARRISON, D., (1978). "Motion of a large gas bubble rising through liquid flowing in a tube", *Journal of Fluid Mechanics*, **89**, 497-514.

COUËT, B. and STRUMOLO, G.S. (1987). "The effects of surface-tension and tube inclination on a two-dimensional rising bubble" *Journal of Fluid Mechanics*, **184**, 1-14.

DAVIES, R.M. and TAYLOR G., (1950). "The mechanics of large bubbles rising through extended liquids and through liquids in tubes" *Proceedings of the Royal Society of London. Series A, Mathematical and Physical Sciences*, **200**, 375-390.

DEBISSCHOP, K.M., MIKSIS, M.J., ECKMANN, D.M., (2002). "Bubble rising in an inclined channel" *Physics of Fluids*, **14**, 93-106.

HUA, J., STENE, J.F., LIN, P., (2008). "Numerical simulation of 3D bubbles rising in viscous liquids using a front tracking method." *Journal of Computational Physics*, **227**, 3358-3382.

HUA, J. and LOU J. (2007). "Numerical simulation of bubble rising in viscous liquid", *Journal of Computational Physics*, **222**, 769-795.

LANGSHOLT, M., ANDERSSON, P., PETTERSEN, B., (2002). "Pipe inclination effects on three-phase slug flow characteristics" IFE report-TP/IFE/003, *IFE/KR/F-2002/064*

MANERI, C.C. and ZUBER, N, (1974). "An experimental study of plane bubbles rising at inclination" *International Journal of Multiphase Flow* **1,** 623-645.

MASLIYAH, J., JAUHARI, R., GRAY, M., (1994). "Drag coefficients for air bubbles rising along an inclined surface" *Chemical Engineering Science*, **49**, 1905-1911.

MIKSIS, M., VANDENBROECK, J.M., KELLER, J.B., (1981). "Axisymmetric bubble or drop in a uniform-flow" *Journal of Fluid Mechanics*, **108**(JUL), 89-100.

PATANKAR, S.V. (1980). "Numerical Heat Transfer and Fluid Flow", Hemisphere, New York.

PESKIN, C.S. (1977). "Numerical-analysis of blood-flow in heart", *Journal of Computational Physics*, **25**(3), 220-252.

RUSCHE, H. (2002). "Computational fluid dynamics of dispersed two-phase flows at high phase fractions", **Ph.D**. thesis, Imperial College of Science, Technology and Medicine.

SHOSHO, E.C. and RYAN M.E., (2001). "An experimental study of the motion of long bubbles in inclined tubes" *Chemical Engineering Science*, **56**, 2191-2204.

TRYGGVASON, G., BUNNER, B., ESMAEELI, A., JURIC, D., AL-RAWAHI, N., TAUBER, W., HAN, J., NAS., S., (2001). "A front-tracking method for the computations of multiphase flow" *Journal of Computational Physics*, **169**, 708-759.

UNVERDI, S.O. and TRYGGVASON, G., (1992). "A front-tracking method for viscous, incompressible, multi-fluid flows." *Journal of Computational Physics*, **100**, 25-37.

VIANA, F., PARDO, R., YANEZ, R., TRALLERO, J.L., JOSEPH, D.D., (2003). "Universal correlation for the rise velocity of long gas bubbles in round pipes" *Journal of Fluid Mechanics*, **494**, 379-398.

WELLEK, R.M., AGRAWAL, A.K., SKELLAND, A.H., (1966). "Shape of liquid drops moving in liquid media" *AIChE Journal*, **12**, 854-862.

WHITE, E.T. and BEARDMORE, R.H. (1962). "The velocity of rise of single cylindrical air bubbles through liquids contained in vertical tubes" *Chemical Engineering Science*, **17**, 351-361.

ZUKOSKI, E.E. (1966). "Influence of viscosity, surface tension and inclination angle on motion of long bubbles in closed tubes" *Journal of Fluid Mechanics*, **25**, 821-837.